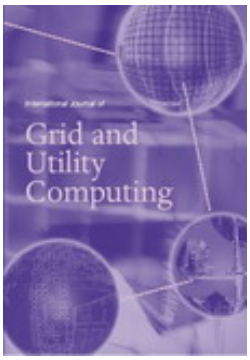

International Journal of Grid and Utility Computing

ISSN online: 1741-8488 - ISSN print: 1741-847X
https://www.inderscience.com/ijguc

Target imaging technology of wireless orbital communication radar

Xin Tan, Chaoqi Wang, Mingwei Wang, Wenyuan Liu, Xianghui Wang

DOI: 10.1504/IJGUC.2023.10059686

Article History:

Received:	07 February 2023
Last revised:	20 March 2023
Accepted:	31 March 2023
Published online:	19 February 2024

Target imaging technology of wireless orbital communication radar

Xin Tan*, Chaoqi Wang, Mingwei Wang, Wenyuan Liu and Xianghui Wang

School of Electronic Information and Artificial Intelligence,
Shaanxi University of Science and Technology,
Xian, Shaanxi, China
and
Shaanxi Artificial Intelligence Joint Laboratory,
Shaanxi University of Science and Technology,
Xian, Shaanxi, China
Email: tanxin@sust.edu.cn
Email: 2933508344@qq.com
Email: wangmingwei@sust.edu.cn
Email: liuwenyuan@sust.edu.cn
Email: wangxh@sust.edu.cn
*Corresponding author

Abstract: With the continuous advancement of technology, non-communication radar imaging is increasingly used in aerial observation and ground observation fields. This article conducts a systematic study on wireless orbit communication radar imaging technology and compensates for deviations in image quality accuracy through motion autofocus. The results show that the video-based backward projection algorithm proposed in this article is better than the RD algorithm and CBP algorithm in identifying large and small corner points. The feature fusion difference test of the rotated convolution unit was conducted on the ResNet18 and VGG16 neural networks and it was found that the recognition rate of the network architecture using the rotated convolution unit was significantly improved. The designed lightweight network based on rotational convolution units has an average recognition rate of 99.48% in the MSTAR data set.

Keywords: wireless communication radar; radar imaging technology; target recognition imaging; SAR imaging; Bayesian imaging.

Reference to this paper should be made as follows: Tan, X., Wang, C., Wang, M., Liu, W. Wang, X. (2024) 'Target imaging technology of wireless orbital communication radar', *Int. J. Grid and Utility Computing*, Vol. 15, No. 1, pp.31–43.

Biographical notes: Xin Tan received his PhD degree from Northwestern Polytechnical University, Xian, China. Now, he works in School of Electronic Information and Artificial Intelligence, Shaanxi University of Science and Technology. His research interests include microwave imaging, array radar microwave signal processing and phased array antenna, etc.

Chaoqi Wang studies in the School of Electronic Information and Artificial Intelligence of Shaanxi University of Science and Technology. The main research interests include microwave imaging, radar array antenna signal processing and application.

Mingwei Wang received his PhD degree from Northwestern Polytechnical University, China. Now, he works in School of Electronic Information and Artificial Intelligence, Shaanxi University of Science and Technology. His research interests include deep learning and artificial intelligence, wireless communication, etc.

Wenyuan Liu received her BEng degree in Communication Engineering from the Taiyuan University of Technology, Taiyuan, China in 2012 and the PhD degree in Microelectronics and Solid Electronics from Tianjin University, Tianjin, China in 2017. Currently, she is a Lecturer with the School of Electronic Information and Artificial Intelligence, Shaanxi University of Science and Technology, Xi'an, China. Her current research interests include neural network-based methods for non-linear microwave device and circuit modelling and their applications in computer aided design for electronic circuits.

Xianghui Wang received his Bachelor's degree in Electronics and Information Engineering from the Xi'an University, Xi'an, China in 2008, the Master's degree in Signal and Information Processing from the Northwestern Polytechnical University (NPU), Xi'an, China in 2011 and the PhD degree in Information and Communication Engineering from the NPU in 2020. He was also a visiting PhD student at the Andrew and Erna Viterby Faculty of Electrical Engineering, Technion – Israel Institute of Technology, Haifa, Israel, between 2016 and 2018. Currently, he is a Lecturer of the School of Electronic Information and Artificial Intelligence, Shaanxi University of Science and Technology, Xian, Shaanxi, China. His research interests include speech enhancement and microphone array signal processing.

1 Introduction

1.1 Background

Since the end of the 20th century, with the increasing complexity of the battlefield environment and the continuous needs of military development, in order to more finely characterise the electromagnetic scattering characteristics of the target, it provides powerful information support for subsequent target detection and recognition. High resolution imaging radar has become an important direction of radar development. As a powerful electronic detection device, radar occupies an extremely important position in the communication field by transmitting and receiving electromagnetic wave signals to detect target position and movement status and other related information. With the continuous development of radar technology, the need for visualisation of radar detection targets has gradually become stronger. For example, in the surveillance and reconnaissance of the battlefield environment, mapping, ship target recognition, ocean currents and glaciers tracking and detection, crop growth monitoring and evaluation and other detection scenarios, it is necessary to obtain detection target images for analysis. In this context, imaging radars have emerged.

1.2 Significance

Only by transmitting a large bandwidth signal can the radar achieve high-resolution imaging in the upward range. When realising high-resolution imaging in the azimuth direction, the target needs to rotate a large accumulated observation angle in the azimuth direction relative to the radar. In actual situations, due to the limitations of radar hardware conditions, the signal bandwidth transmitted by the radar is limited and at the same time we cannot artificially increase the effective rotation of the target in the azimuth direction. In addition, the sampling rate is twice the bandwidth, so more data needs to be sampled. This puts a great burden on the storage and transmission of hardware, so how to use less echo observation data to achieve high-resolution radar imaging becomes particularly important. In summary, the research and optimisation of radar imaging technology is of great significance to target reconnaissance and detection.

1.3 Related work

Wireless orbital communication radar target imaging technology has broad application prospects. Therefore, this technology has been a research hotspot in the field of monitoring and remote sensing in recent years, and many people have conducted research on it. Banerjee et al. (2016) proposed that due to the advancement of wireless communication systems, railways, academia, related industries and standards bodies and even the European Space Agency, have all participated in the development of HSR's highly interconnected train communication system. To jointly realise the ability to provide uninterrupted high-speed fault-tolerant communication networks on the wireless track, Banerjee et al.'s (2016) survey provides an overview of the current technical level and future trends of wireless technology, aiming to realise the concept of HSR communication services. However, the content outlined is relatively general and lacks systemicity. Liu et al. (2016) mainly studied the design of broadband multi-input multi-output radar waveforms and its application in multi-target imaging. They established an unconstrained optimisation model based on joint minimisation of beam pattern and power spectrum matching errors. Numerical results show that this method can approximately achieve the desired multi-beam and power spectral density. Using the sparse representation method, the designed randomly distributed power spectrum waveform can be applied to multi-target imaging (Liu et al., 2016). Their research has very high-application value, but the implementation method is too complicated. Wang and Chen (2019) proposed a new three-dimensional ISAR imaging method. First, the high-precision gradient adaptive algorithm is used to reconstruct the range-dimensional echo, and then the method of minimising the entropy of the average range distribution is used to estimate the parameters used to compensate the translation component of the received echo. In addition, through the joint phase auto-focusing method, the phase adjustment and image registration of the sparse echo are realised. Finally, combine the distance measurement and interference processing of ISAR images to reconstruct the three-dimensional geometric coordinates of the two-dimensional sparse ship target (Wang and Chen, 2019). Their research algorithm is more practical and effective when the received echo is two-dimensional, but the

specific application effect is not yet known. Zhang et al. (2018) proposed a resident scheduling algorithm for the resource allocation problem of digital array radar. First, the comprehensive priorities of different radar tasks are designed to ensure imaging and tracking search tasks, and then the radar resource optimisation scheduling model is established according to the pulse interleaving constraints. Finally, a heuristic algorithm is used to solve the problem, and sparse cognitive ISAR is used to achieve accurate tracking of the target part (Zhang et al., 2018). Their algorithm can not only improve the performance of the radar system, but also produce satisfactory imaging results. Sun et al. (2019) proposed an improved limited Broyden-Fletcher-Goldfarb-Shanno particle swarm optimisation algorithm to solve the problem of slow imaging speed and poor reconstruction accuracy under the condition of blurred wall parameters. The combination of this algorithm and the block orthogonal matching and tracking algorithm can not only accurately reconstruct the position of the side wall, but also accurately reconstruct moving and stationary targets using multipath information. Compared with the traditional BFGS algorithm and particle swarm algorithm, this algorithm can reduce the calculation time and provide more accurate estimation results (Sun et al., 2019). The algorithm has good performance, but the specific implementation method of the algorithm in his research is not clear enough. Comite et al. (2017) proposed a multi-view ground penetrating radar target detection method, which uses a tomographic algorithm that takes into account the near-field properties of the sensing problem to generate various images corresponding to different views. In addition, in order to reduce clutter and maintain high span-distance resolution on the imaging area, each image is calculated in a piecewise manner using coherent integrals on suitable measurement sets from multiple platform positions. Finally, two fusion methods based on likelihood ratio test detectors are used to combine multi-view images to enhance target detection (Comite et al., 2017). Their experiment proved that the multi-view method is better than the single-view imaging performance, but this method is not suitable for practical promotion and is more troublesome to operate.

1.4 Innovation

Wireless orbital communication radar technology is widely used in target monitoring, positioning and tracking and has gradually developed to the imaging and recognition of a variety of coordinated and non-coordinated targets, with strong information acquisition capabilities. However, based on its imaging characteristics, there will still be problems such as low target recognition accuracy and serious focus shifting. This article has conducted research on the above part of the content, the novelty of the article mainly lies in: (1) The innovation of wireless communication radar imaging technology. In order to be able to perform high-efficiency imaging of video sequences, this paper proposes a new video-based backward projection algorithm, which can filter out meaningless information. (2) Innovation of radar imaging network architecture, the article conducted a comparative experiment on the feature recognition difference between not using and using the rotating convolution unit, and found that the feature recognition rate of the network architecture using the rotating convolution unit would be higher. At the same time, a lightweight neural network structure with fewer network levels and simplified structure is proposed for small batch sample sets. The results verify that the network can achieve high-recognition accuracy.

2 Target imaging technology of wireless orbital communication radar

2.1 Principle of SAR imaging of wireless communication radar

According to different working methods, imaging radars are divided into two categories: Synthetic Aperture Radar (SAR) and Inverse Synthetic Aperture Radar (ISAR). Among them, SAR is generally used for space-borne and airborne observations, and ISAR is generally used for ground-based radar observations. The imaging principles of the two are the same. They both use the relative motion between the radar and the target to image. The difference is that SAR is radar moving but the target does not move. ISAR means the radar does not move but the target moves, so it is called 'inverse'. Since the two types of imaging principles are the same, and SAR is more suitable for simulation experiments, the main test object in this article is SAR and some experiments have also studied ISAR.

Synthetic Aperture Radar (SAR) is a high-resolution imaging sensor that maps the electromagnetic scattering characteristics of a target into a two-dimensional image in the range and azimuth direction (Smys et al., 2019). Owing the strong transmission of electromagnetic waves, SAR is not affected by weather factors such as clouds, rain, snow, fog and environmental factors such as day and night, light and darkness, and can continuously observe the target area all day long.

In radar imaging, the direction of movement of the carrier aircraft is defined as the azimuth direction, and the direction perpendicular to the direction of movement is defined as the distance direction (Jiang et al., 2016). When imaging a ground target, the transmitter transmits a repetitive pulse signal to the ground observation zone. After a certain time delay, the radar echo signal with the target information to be measured is collected, and the scattering coefficient is extracted. According to the distance and azimuth dimension display, a two-dimensional radar image is finally obtained. This article takes airborne radar as an example. The geometric model of airborne SAR movement is shown in Figure 1.

2.2 Wireless communication radar target imaging algorithm

(1) *Range Doppler algorithm*: As a classic radar imaging algorithm, the RD algorithm can be understood as the evolution of the two-dimensional matched filtering

algorithm in the time domain. Its sub-dimension processing feature improves the efficiency of SAR imaging processing, and it is often combined with high-performance processors such as FPGA to achieve high-resolution and high-speed imaging in imaging modes with high real-time requirements (García-Rial et al., 2020). The RD algorithm mainly includes three steps of distance compression, distance walking correction and azimuth compression. The specific flow chart is shown in Figure 2.

Figure 1 Geometry model of airborne frontal SAR

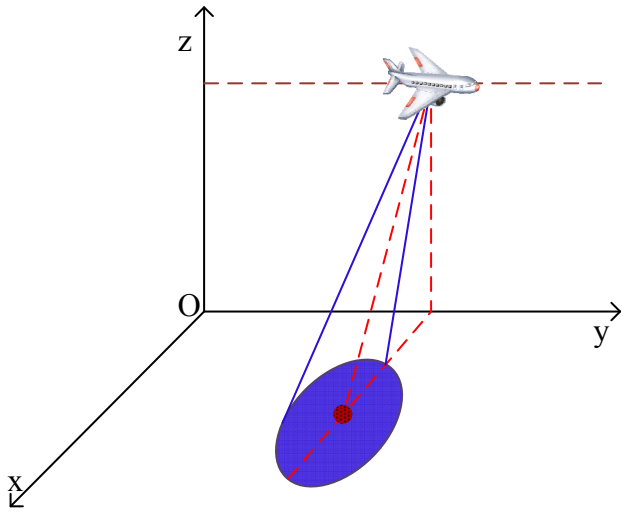

Figure 2 RD algorithm flow

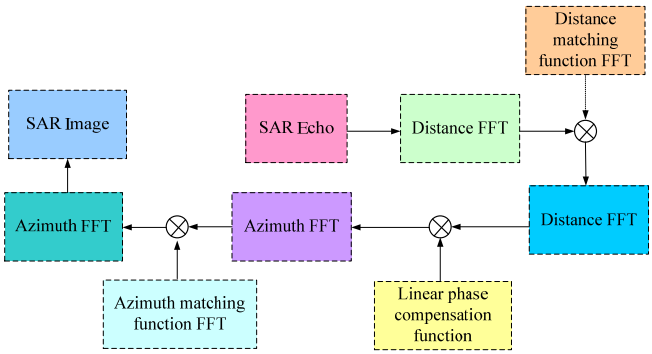

The essence of pulse compression is to perform matched filter output on the echo signal. Here, Fourier transform FFT is used as equation (1) and the range window function $b_s(t_m)$ is added. The range pulse compression processing SAR echo signal is shown in equation (a) (Yurduseven et al., 2019). In the formula, Δf_s is the chirp signal band, D is the amplitude of the point target signal after range compression and $\sin c$ is the influence of range migration on the delay of the echo packet; the distance migration correction needs to be multiplied by the linear phase function $F = e^{-j\frac{4\pi}{\lambda}\frac{(vt_m)^2}{2S_O}}$ that compensates the distance migration. The fast-distance time-azimuth full time domain signal after compensation for distance migration is equation (b) (Narayanan et al., 2019).

$$A(t,t_m,S_O) = IFFT\left\{FFT\left[A(t,t_m,S_O)\right]\cdot FFT\left[A_s(t)\right]\right\} \quad (1)$$

$$\begin{cases} A(t,t_m;S_O) = \\ D\sin c\left[\Delta f_s\left(t-\dfrac{2S(t_m;S_O)}{c}\right)\right]b_s(t_r)e^{-j\frac{4\pi}{\lambda}S(t_m;S_O)} \quad (a) \\ A(t,t_m;S_O) = \\ D\sin c\left[\Delta f_s\left(t-\dfrac{2S(t_m;S_O)}{c}\right)\right]b_s(t_r)e^{-j\frac{4\pi}{\lambda}\left(S_O+\frac{(vt_m)^2}{2S_O}\right)} \quad (b) \end{cases} \quad (2)$$

Finally, the azimuth matched filter function is used to compress the azimuth, and the focused point target is obtained as shown in equation (3), where Δf_s is the Doppler bandwidth, and the azimuth matched filter function is the same as the range pulse compression processing (Tang et al., 2017).

$$\left\{A_b(t,t_m;S_O) = H\sin c\left[\Delta f_s\left(t-\frac{2S_O}{c}\right)\right]\sin c\left(\Delta f_s t_m\right)\right. \quad (3)$$

(2) *Back projection algorithm*: The BP algorithm can choose the projection space arbitrarily according to the demand, and generally also choose the range-azimuth imaging space. The schematic diagram of the algorithm is shown in Figure 3, the specific algorithm flow is:

a) Grid division, the grid interval should be less than the theoretical resolution;

b) Calculate the instantaneous slope of the imaging space pixel unit and the antenna phase centre; for the pixel unit O, the distance history at time t can be calculated by formula (4).

$$R(t,O) = O(t) - O_{o2} \quad (4)$$

c) Calculate the time delay and obtain the echo data; the time delay of the pixel unit O at time t is:

$$\tau(t,O) = 2R(t,O)/c \quad (5)$$

d) Compensate the Doppler phase of all pixel units, and perform coherent superposition of the echo data, and repeat the above steps until all the units are traversed and processed.

Figure 3 Back projection algorithm

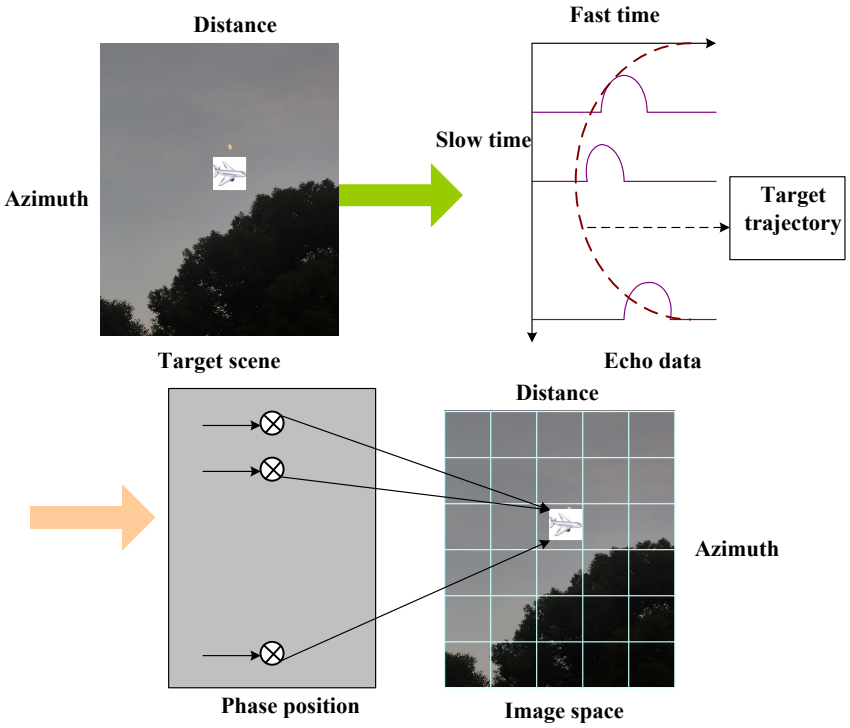

In order to realise the continuous recognition and observation of the target in the area, it is generally necessary to use continuous multi-frame images of video imaging. The BP algorithm has the characteristics of pulse-by-pulse processing and superposition, which can image and store sub-image pixel data through short sub-holes and then perform sliding-window superposition to avoid repeated data processing. It can be improved to a video-based backward projection algorithm while reducing costs. The algorithm flow is shown in Figure 4.

Figure 4 Schematic diagram of video imaging (see online version for colours)

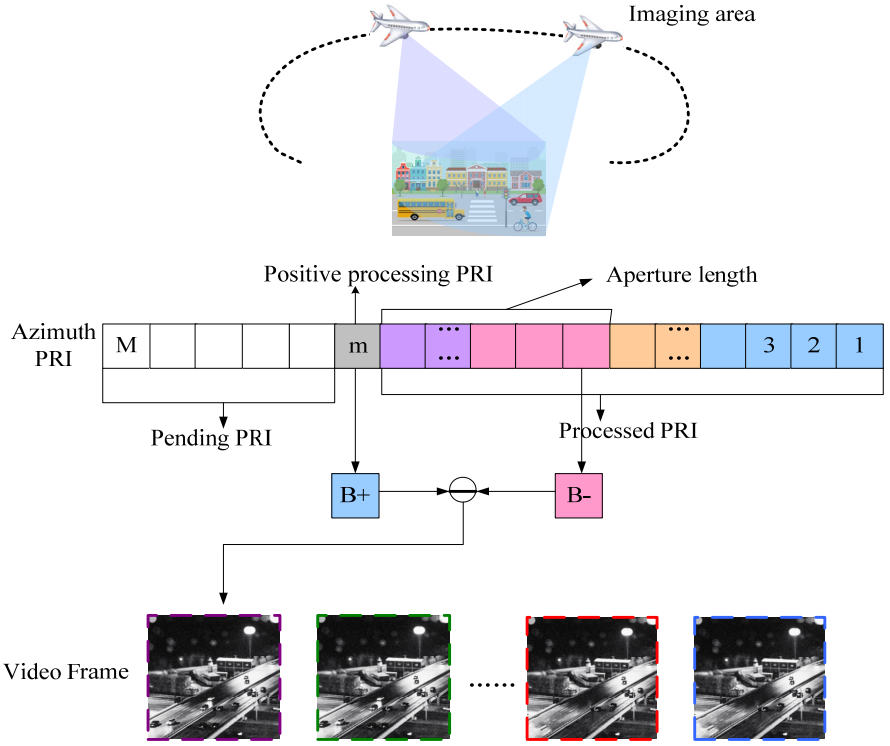

(3) *Convolution back projection algorithm*: The convolution-inverse projection algorithm originated from tomography technology (CT technology), which uses CT technology and is similar to the turntable imaging model and is applied to the field of SAR imaging based on the projection slice theorem (Ng et al., 2017). The projection line is perpendicular to the LOS of the turntable, and the position of the projection line is different according to the position of different *w*-values. The Randon transformation of the scattering function is:

$$C_{\vartheta}(w)=\int_{-\infty}^{\infty} f(t\cos\vartheta-w\sin\vartheta,t\sin\vartheta+w\cos\vartheta)\,dt \tag{6}$$

Perform one-dimensional Fourier transform to obtain equation (7), it can be seen that the one-dimensional transform of the projection value of the reflection function is a slice of the two-dimensional Fourier transform of the reflectance function $f(x,y)$ under the angle (Yong et al., 2017).

$$\begin{cases}\widehat{C_{\vartheta}}(b)=\int_{-\infty}^{+\infty} C_{\vartheta}(w)\exp(-j2\pi bw)\,dw\\ \quad\int f(t\cos\vartheta-w\sin\vartheta,t\sin\vartheta+w\cos\vartheta)\exp\\ \quad(-j2\pi bv)\,dtdw\\ \quad=G(b\cos\vartheta,b\sin\vartheta)=G(b,\vartheta)\end{cases} \tag{7}$$

The CPB algorithm recovers the two-dimensional SAR image through the backscattered field of the target acquired by the radar at different angles, and uses the formula derived from the turntable imaging to set $b=2f/c$, $G(b,\vartheta)=E_s(b,\vartheta)$, then we can get:

$$f(x,y)=\int_{\vartheta_{\min}}^{\vartheta_{\max}}\int_{b_{\min}}^{b_{\max}} bG(b,\vartheta)\exp\left[j2\pi b(y\cos\vartheta-x\sin\vartheta)\right]dbd\vartheta \tag{8}$$

Regarding the integral of *b* in the above formula as the inverse Fourier transform of the parameter $q=y\cos\vartheta-x\sin\vartheta$, then formula (8) can be decomposed, $F_{\vartheta}(q)$ is the radar target projection value, *b* is the spatial frequency and the decomposition result is:

$$F_{\vartheta}(q)=\int_{b\min}^{b\max} bG(b,\vartheta)\exp(j2\pi bq)\,db \tag{9}$$

$$f(x,y)=\int_{\vartheta\min}^{\vartheta\max} F_{\vartheta}(q)\,d\vartheta \tag{10}$$

2.3 Radar target imaging echo model

(1) *Target echo model*: When the radar is working, it is generally in front-view or squint mode, and the radar beam is dynamic throughout the imaging process. No matter which mode it is in, the radar transmitting signal and receiving signal model are consistent. Generally speaking, the linear frequency modulation signal transmitted by the SAR system can be expressed by the formula, where T_m is the pulse time (transmission signal pulse width), *t* is the fast time and K_s and g_0 are the signal frequency modulation slope and carrier frequency slope, respectively, $w_s(t)$ is the pulse envelope, which can be approximated by the rectangular function (11) (Kang et al., 2016).

$$F_s(t)=w_s(t)\exp\left\{j2\pi\left(g_0t+\frac{K_st^2}{2}\right)\right\},\quad t\in[-T_m/2,\ T_m/2] \tag{11}$$

$$w_s(t)=rect(t/T_m) \tag{12}$$

For any point d_s in the observation area, if (x,y,z) is the position of the radar antenna and the coordinates of the scattering point d_s are (x_s,y_s,z_s), then the distance between the scattering point and the radar antenna is:

$$R(d_s)=\sqrt{(x-x_s)^2+(y-y_s)^2+(z-z_s)^2} \tag{13}$$

c is the speed of light, the backscatter coefficient of d_s is σ_s and the received echo signal can be expressed as:

$$F_s(t,d_s)=\sigma_s\exp\{-j4\pi R(d_s)/\lambda\}\cdot\exp\left\{j\pi K_s\left(t-\frac{2R(d_s)}{c}\right)^2\right\} \tag{14}$$

Finally, the radar echo of the imaging area at a certain receiving moment can be obtained as equation (15), where ROI is the imaging area, which is a fixed area determined by the beam width.

$$\begin{aligned}F_s(t)&=\sum_{s\in ROI}F_s(t,\ d_s)\\&=\sum_{s\in ROI}\sigma_s\exp\{-j4\pi R(d_s)/\lambda\}\cdot\exp\left\{j\pi K_s\left(t-\frac{2R(d_s)}{c}\right)^2\right\}\end{aligned} \tag{15}$$

(2) *Correlative imaging echo model of moving target*: The radar correlation imaging technology can improve the super-resolution performance and anti-jamming ability of radar, which is an extension of optical imaging theory (Bichi et al., 2022). This technology transmits a set of time-independent and mutually orthogonal signals through a radar array, and can form a detection signal with time-independent and space-independent in the radar detection target area. The spatial distribution of the scattering intensity of the target can be obtained through the correlation processing of the detection signal and the received signal (Wang et al., 2018).

As shown in Figure 5, *Y* is the distance direction and *X* is the azimuth direction. It is assumed that the radar associated imaging model system has *R* transmitting signal units and *N* receiving units. If the *r*-th transmitting unit transmits a signal

of $A_{tr}(t)$, in order to meet the independent condition, the transmitted signal must be as random as possible (Li et al., 2017). The linear combination of the emitted signals emitted by the R emission signal units to any point in the imaging area, here becomes a random radiation field as shown in equation (16) (Yong and Li, 2016). Where s is the position vector from the origin to the target, O is the detection area and is the position vector from the i-th radar transmitter to the origin of the coordinates.

$$A_O(s,t) = \sum_{i=1}^{R} A_{ti}\left(t - \left(\overline{s} - \overline{S_i}\right)/c\right) \tag{16}$$

Figure 5 Radar correlation imaging echo model

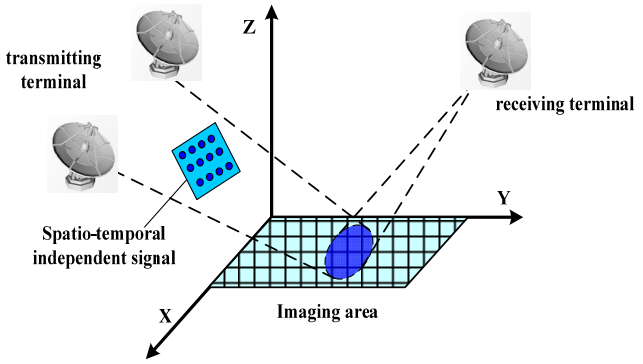

Assuming that the scatter function of the scatterer in the detection target area is $\delta(d,\vartheta)$, and $\overline{S_s}$ is the distance from the origin of the coordinates to the radar signal receiving end, the echo received by the radar is:

$$A_s(t) = \int \delta(s,\vartheta) A_O\left(\overline{s}, t - \left(\overline{s} - \overline{S_s}\right)/c\right) ds \tag{17}$$

Since the radar detection signal is not correlated in the time domain, the correlation function value of the radar echo signal and the reference signal at a certain point in the radar detection area can be calculated, and the scattering coefficient of any target in the imaging area can be obtained as:

$$\delta_s = \frac{\int A_s(t) A_O^*(s,t)\, dt}{R} \tag{18}$$

The space-independent features of microwave signals are not suitable for extracting radar detection target information, and radar associated imaging requires corresponding algorithms to reconstruct high-resolution target images. At the same time, the time delay from the target to the receiver needs to be corrected (Yang et al., 2016). For discrete signals, assuming that the area is divided into M grids and the target scatterer is considered to be at the centre of the grid, the echo signal can be expressed as:

$$A_s(t) = \sum_{j=1}^{M} \delta_j A_O\left(\overline{s}, t - \left(\overline{s} - \overline{S_s}\right)/c\right) \tag{19}$$

The number of echo signal sampling points is N, and the discrete model $b = V\delta$ can be obtained. Then the radar model reference matrix based on associated imaging is:

$$V = \begin{bmatrix} A_O(\overline{s_1}, t_1 - (\overline{s_1} - \overline{S_s})/c & \cdots & A_O(\overline{s_M}, t_1 - (\overline{s_M} - \overline{S_s})/c \\ A_O(\overline{s_1}, t_2 - (\overline{s_1} - \overline{S_s})/c & \cdots & A_O(\overline{s_M}, t_2 - (\overline{s_M} - \overline{S_s})/c \\ & \cdots & \\ A_O(\overline{s_1}, t_{N-1} - (\overline{s_1} - \overline{S_s})/c & \cdots & A_O(\overline{s_M}, t_{N-1} - (\overline{s_M} - \overline{S_s})/c \\ A_O(\overline{s_1}, t_N - (\overline{s_1} - \overline{S_s})/c & \cdots & A_O(\overline{s_M}, t_N - (\overline{s_M} - \overline{S_s})/c \end{bmatrix} \tag{20}$$

In the radar associated imaging system, the radar associated imaging uses orthogonal waveforms to increase the spatial diversity of the detection signal. The transmitted signal of the radar is a time-space uncorrelated signal, and then the echoes returned by the scatterers at different positions are also space-time independent, and the scatterer echoes are distinguished according to the waveform difference of the scatterer echoes to obtain the target image. This greatly improves the resolution in the radar beam.

2.4 Improved image quality of radar imaging

(1) *Motion compensation self-focusing algorithm*: In the signal reception process, the SAR system is not completely idealised, so there is a certain phase error in the echo data, which will cause the SAR image to not be well focused (Qian et al., 2018). Self-focusing technology is used to correct image phase errors.

The phase error function is usually modelled by a one-dimensional function of Fourier phase added to the imaging data (Peng et al., 2019). First, perform the inverse discrete Fourier transform on the sample points of a SAR image, and the result is equation (21) (Singh et al., 2022). Where k is the Doppler frequency index variable, x and y are the distance and azimuth directions, Y represents the number of samples in the azimuth direction and $\tilde{A}_{xk}$ and A_{xy} are a pair of Fourier transform pairs.

$$A_{xy} = \sum_{k=0}^{Y-1}\left[\tilde{A}_{xk} \cdot \exp\left(\frac{j2\pi ky}{Y}\right)\right] / Y \tag{21}$$

Image defocusing caused by phase error generally occurs in the data acquisition process. Set the correction error function is $\sigma(k)$, then the corrected image B_{xy} is:

$$B_{xy} = \sum_{k=0}^{Y-1} \exp\left[j\left(\frac{2\pi ky}{Y} - \sigma(k)\right)\right] \cdot \tilde{A}_{xk} / Y \tag{22}$$

When the phase error of each sub-aperture satisfies the quadratic function model, k_0 is a known function and d is an unknown parameter related to the aperture centre to determine the curvature of the quadratic curve, the correction function can be written as:

$$\sigma(k) = d\left(k - k_0\right)^2$$

The unknown parameter d can be solved by minimising the entropy of the SAR image, which is defined as:

$$\varphi(d) = \left[E_z \sum_{xy} \left|Z_{xy}(d)\right|^2 \left[\ln\left|Z_{xy}(d)\right|^2\right]\right]^{-1} + \ln E_z \tag{24}$$

When the entropy value is smaller, the image stability is stronger. The following solves the quadratic term coefficient corresponding to the minimum entropy value, and the target value is equation (25), while satisfying equation (26) (Long et al., 2019).

$$d_{apt\_r} = \arg\min \varphi(d) \tag{25}$$

$$\varphi\left(d_{apt\_r}\right) = 0 \tag{26}$$

3 Experiment

3.1 Radar imaging target recognition simulation experiment design

(1) *Simulation system*: In this section, simulation experiments are used to verify the performance of the proposed algorithm and image enhancement experiments. The synthetic aperture radar SAR simulation data set is used for experimental analysis, and a single-antenna SAR system working in strip mode is used. The relative target angle of radar is between 0° and 360°, and the system parameters are shown in Table 1.

Table 1 Simulation system parameters

Carrier frequency	*Pulse repetition rate*	*Platform height*	*Platform speed*
25 GHZ	1800 Hz	8000 m	280 m/s
Bandwidth	Adjacent Pulse Interval	Squint Angle	FPS
2 GH	560	45°	1

(2) *Experimental arrangement*: First, the algorithm comparison of several radar imaging algorithms mentioned in the previous article is carried out. Secondly, in order to verify the performance of the video SAR back-projection algorithm based on the extension of the BP radar imaging algorithm in this paper, this paper first carried out the SAR target classification and angle estimation experiment based on the basic neural network, then, the feature recognition rate experiment was carried out for several other network architectures; at the same time, a lightweight neural network is proposed and the feature recognition difference test of the rotating convolution unit is carried out. After that, for image quality improvement and image enhancement, a tracking experiment and a trajectory optimisation experiment were carried out using the self-focusing algorithm. Finally, the content of this experiment was summarised and analysed.

3.2 Performance of radar imaging algorithm

(1) *Comparison of imaging algorithms for wireless communication radars*: For range Doppler RD algorithm, back projection BP algorithm, convolution back projection CBP algorithm and video BP algorithm based on convolution back projection (v-BP), in order to illustrate the differences in the application of the four types of algorithms in the large-angle SAR imaging model, this paper performs SAR imaging on the scattering centre model with parameters (the amplitude of the scattering centre is 1.3 V/m; the signal band: 2.28–19.28 GHz; the scanning angle is: θ=90°Φ=390°; the interval frequency is 50 MHz; the angular interval is 1.2°; the position information is (0, 0.09), (0, 0.12), (0, 0.15), unit m;). The SAR azimuth images based on the four algorithms are shown in Figure 6. The distance between the three-scattering centres in the azimuth direction is 0.03 m. According to the results shown in the Figure 6, the range Doppler RD algorithm is completely invalid. The video BP algorithm V-BP algorithm based on convolution back projection, which is extended in this paper, has the highest resolution, followed by BP algorithm and then convolution back projection algorithm.

Figure 6 Azimuth of the scattering centre (see online version for colours)

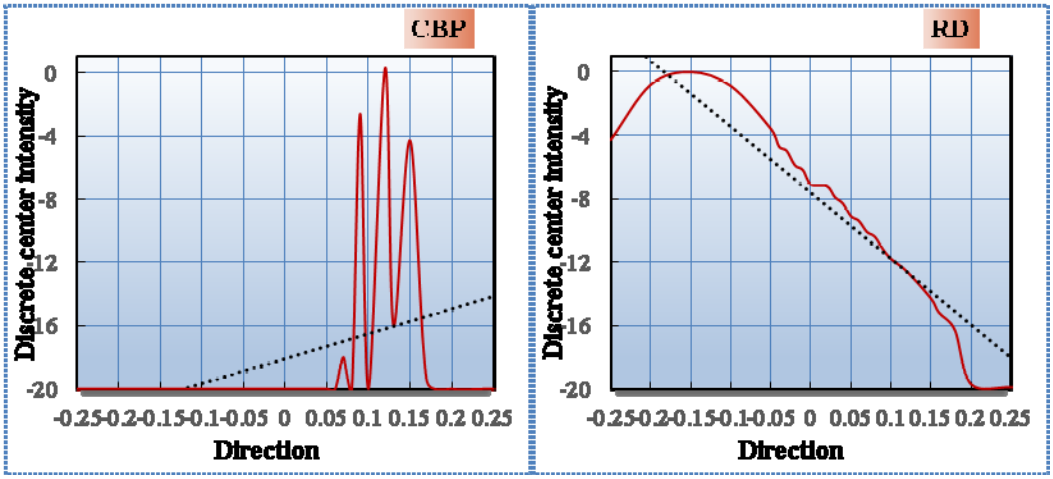

Figure 6 Azimuth of the scattering centre (continued) (see online version for colours)

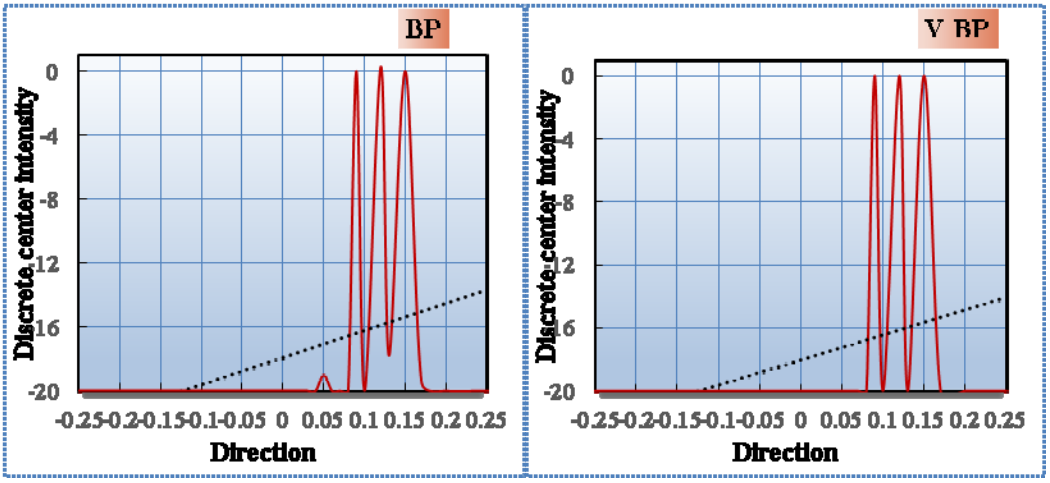

In addition to the difference comparison in the application of large corners, the performance of the algorithm needs to be compared with the calculation efficiency. Here, the time of several algorithms for small-turn and large-turn imaging scene conditions are respectively counted, and the results are shown in Figure 7. It can be concluded from Figure 7 that the RD algorithm has the fastest calculation speed due to the use of Fourier transform; the CPB algorithm may have an interpolation process, so the efficiency is in the middle; the PB algorithm and the improved V-BP algorithm in this article have the slowest calculation efficiency.

Based on the above experiments, several algorithms are comprehensively analysed. In terms of imaging effects, the range Doppler RD algorithm is invalid for the large-angle imaging model. The video BP algorithm based on convolutional back projection proposed in this paper has the best imaging effect because it filters the repetitive imaging information. In terms of algorithm efficiency, the operating efficiency of RD is the highest. The algorithm in this paper is relatively slow, but it also meets the experimental requirements.

(2) *SAR target classification and angle estimation of wireless communication radar*: The radar target recognition simulation data set contains three types of recognition targets. The three types of aircraft models are represented by M1, M2 and M3, respectively. The geometric structures of the three aircraft models are shown in Figure 8. These target parameters are shown in Table 2. The experiment uses electromagnetic simulation software FEKO, calculates the target by geometric optics method to obtain electromagnetic scattering data and then performs echo simulation and imaging processing. The simulated radar works in the *X*-band, adjusts the radar incidence angle and target speed parameters and obtains sample images under different imaging conditions. The ratio of the experimental training set to the test set is 1:1.

Figure 7 Calculation efficiency statistics

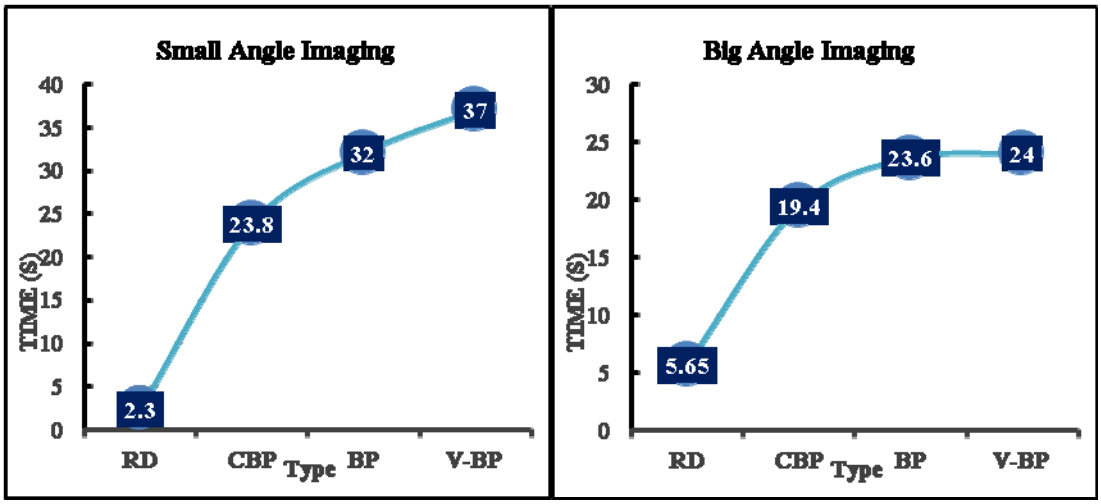

Figure 8 Aircraft model geometry

Table 2 Radar target recognition simulation moving target parameters

Target	*Positioning position (x, y)*	*Distance velocity (m/s)*	*Azimuth velocity (m/s)*	*Test quantity*
M1	(8000, 0)	28.2690	18.4681	289
M2	(4600, 50)	39.4126	21.0486	292
M3	(5200, 0)	66.5391	34.8549	291

In the experiment, the benchmark network is trained first, and then the training parameters are transformed into the kernel mapping by shifting and loaded into the convolutional backward projection neural network, and the data of different angles are transformed for testing. The experimental results are shown in Figure 9. It can be concluded that the projection BP algorithm after video convolution can achieve high-precision classification of SAR data. Figures 9(①) and9(④) are data maps with target angles of 0° and 180°, respectively, with an accuracy rate of 100%. When the target angles are 90°, 225° and 270°, as shown in Figures 9(③), 9(⑤) and 9(⑥), the accuracy rates are respectively 93%, 95% and 96%. Figure 9(②) is the result when the target angle is 45°, 23% of M1 is recognised as M2.

Figure 9 Confusion matrix of classification results from different angles (see online version for colours)

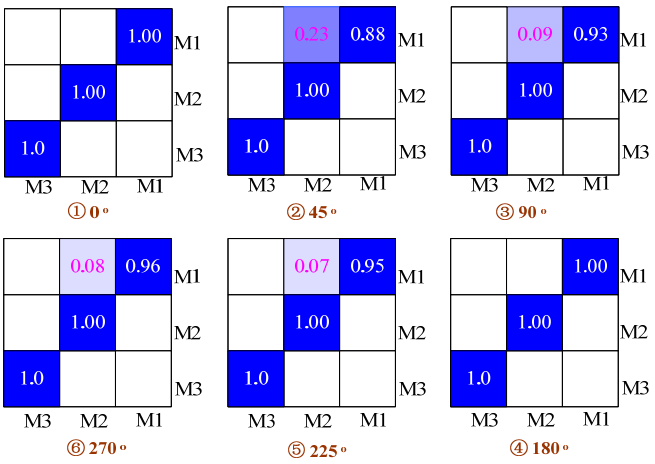

(3) *Neural network feature recognition rate experiment*: The neural network feature recognition experiment is carried out on the two benchmark neural network architectures ResNet18 and VGG16. The structure of ResNet18 is an 18-layer network with weights, including a convolutional layer and a fully connected layer, excluding the pooling layer and the BN layer. The VGG16 structure has 13 convolutional layers and 3 fully-linked layers. The MSTAR database is used here as a data set collection library for SAR image automatic target recognition research. The database contains a variety of ground target airborne SAR imaging results, and the radar relative target angle of view is from 0 to 360°. In this section of the experiment, 6 types of targets are selected for recognition and verification. The training set and test set information are shown in Table 3.

Table 3 MSTAR data set information

Target type	*Number of training samples*	*Number of test samples*
BTR60	286	274
T62	283	273
ZLL131	287	271
BMP2	231	193
2S1	283	274
D70	288	273

1) *Feature fusion difference experiment of rotating convolution unit*: In the experiment, in order to verify the difference of the feature fusion method after rotating the convolution unit, each network (ResNet18, VGG16) built three different networks. They are a reference network without adding a rotating convolution unit, a network using a convolution unit and using Ti-pooling feature fusion and a network using a convolution unit using Add-pooling fusion. Ti-pooling (Transformation-invariant pooling) is similar to maximum pooling, which can effectively extract the salient features of the output target, but it is also easy to cause the loss of insignificant features. Add-pooling is an algorithm based on Ti-pooling that replaces the maximum operator with an addition operation during network design. The average recognition rate results of 25 trainings are shown in Figure 10.

As shown in Figure 10, through comparison, it can be concluded that the use of the rotating convolution unit can effectively improve the network classification performance of the two different networks, ResNet18 and VGG16, when there are fewer training samples. And the smaller the sample set, the higher the performance gain that its feature augmentation function will bring to the network. In addition, comparing different feature fusion methods of the same network, it can be concluded that the performance of Add-pooling is better than Ti-pooling.

Figure 10 Two network model training recognition rate curves (see online version for colours)

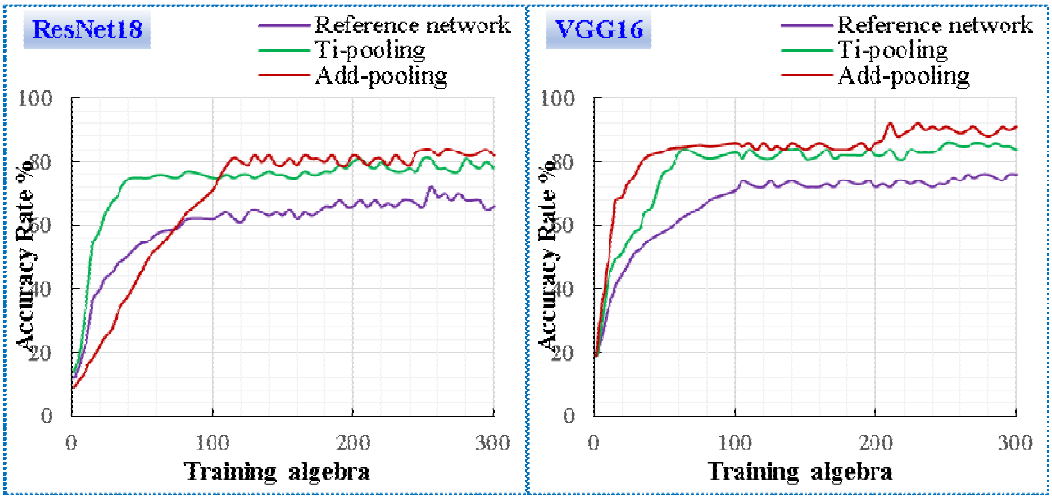

2) *Lightweight neural network convolution unit feature recognition difference test*: Since the data set has fewer than 300 samples of each type and is distributed in different imaging perspectives, this paper designs a lightweight network based on a rotating convolution unit with a small number of layers. The last convolutional layer of the network is the output layer to replace the fully connected layer in the general classification network. The test results of the network after training with different numbers of samples are shown in Figure 11, Num refers to the number of sample sets and Num-100 refers to 100 training samples for each type of recognition target. It can be seen that although the number of lightweight network layers is small and there is no complex convolution structure, the classification performance is still very good. When each class is trained with 25 samples, the recognition rate is higher than the ResNet18 and VGG16 architectures in the previous section, the recognition rates when using Ti-pooling and Add-pooling are 88.9% and 90.01%, respectively.

Figure 11 Lightweight convolutional unit network recognition degree (see online version for colours)

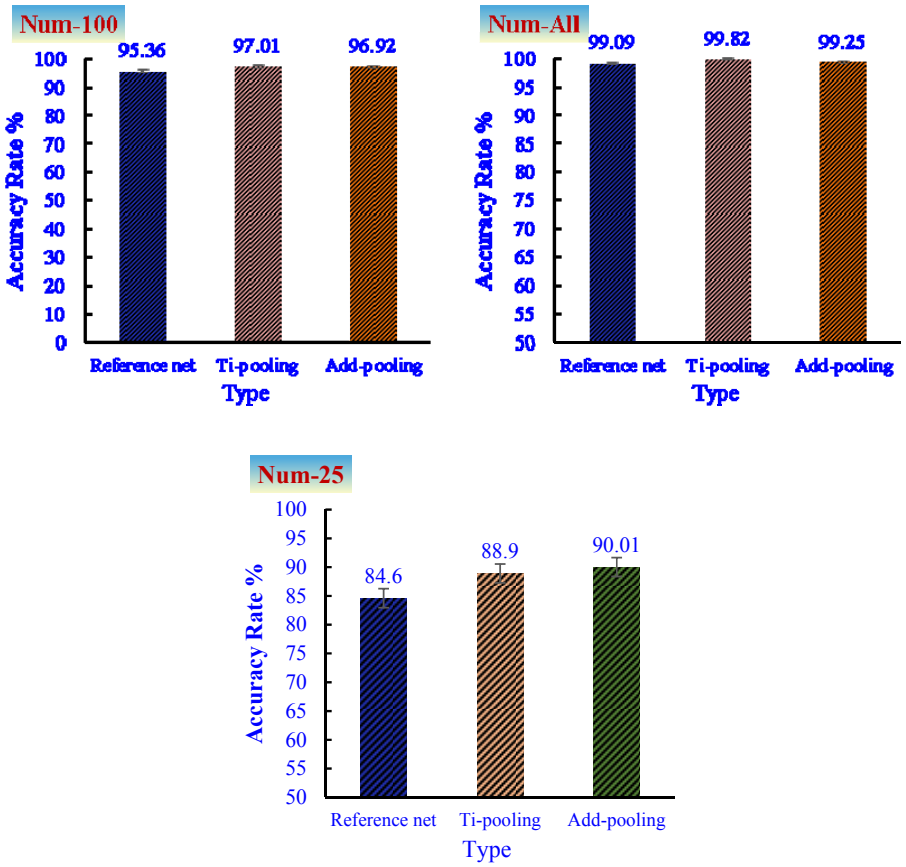

The increase in the number of samples will reduce the gain performance of the convolution unit, but here when the number of samples of each type is all, the lightweight network based on the convolution unit still has a recognition rate gain of 0.49%. The classification results of the light-weight convolutional unit network for the six types of MSTAR data sets are shown in Table 4. Obviously, the classification and recognition effect of this network for BTR60, T62, ZLL131 and D70 is very good, the recognition rate reaches 100% and the total average recognition rate is also 99.48%.

Table 4 Lightweight network recognition results

Type	*BTR60*	*T62*	*ZLL131*	*BMP2*	*2S1*	*D70*	*Discrimination*
BTR60	274	–	–	–	–	–	100%
T62	–	273	–	–	–	–	100%
ZLL131	–	–	271	–	–	–	100%
BMP2	–	–	–	188	4	–	97.3%
2S1	–	–	–	1	273	–	99.6%
D70	–	–	–	–	–	273	100%
Average				99.48%			

3.3 Experimental results of motion compensation self-focusing image enhancement

The SAR system works in the *X*-band, the image resolution is 0.4 metres and the selected image size is 3000 (azimuth) and 3000 (range), the experimental results of motion compensation self-focusing image enhancement are shown in Figure 12. The comparison of the two pictures in Figure 12 shows that the SAR in Figure 12(①) is not compensated for phase error, and there is a lot of defocus in the image, which makes it difficult to identify roads, buildings and pedestrians and the overall effect of the image is seriously degraded. Figure 12(②) is the motion error self-focusing compensation. It is obvious from the visual that the image quality has been greatly improved, showing a better focusing effect and the road becomes very clear. This picture can show that the motion compensation self-focusing technology has a great effect on improving the defocusing problem of radar SAR imaging images.

Figure 12 Comparison before and after motion compensation

① ②

4 Discussion

The main research content of this paper is the target imaging technology of wireless communication radar. With synthetic aperture radar as the main research object, the radar imaging algorithm and image enhancement algorithm are experimentally studied. The article first introduces wireless communication radar SAR imaging principles, characteristics and main application directions; secondly, it summarises several algorithms for wireless communication radar target imaging, including RD algorithm, BP algorithm and CBP algorithm. In addition, a video back projection algorithm based on the BP algorithm is proposed; then the echo model of radar target imaging and the radar imaging image enhancement algorithm are summarised, showing some previous research results.

In the course of the experiment, this article first compares the performance of various algorithms. In terms of comprehensive performance, the recognition performance of the video backward projection algorithm proposed in this article is better. Secondly, a comparative analysis of the difference between using convolution unit and not using convolution unit is carried out, and a lightweight neural network is proposed based on a small sample set. The average recognition rate of the lightweight neural network in the simulation experiment has reached more than 99%, and the performance is the best among the several network architectures in this experiment. Finally, experiments are carried out on the effect of the motion compensation self-focusing algorithm applied to the wireless communication radar target recognition. The results show that the compensated image has a significantly improved focusing effect.

5 Conclusion

The wireless communication radar SAR imaging target recognition system has very broad application and development prospects in the field of remote sensing and intelligent monitoring technology, and it occupies an important position in both military and civilian applications. In actual situations, due to the uncertainty of moving targets, the complexity of the background and targets and the real-time nature of information transmission, SAR imaging technology needs to meet actual needs with higher standards and requirements. This paper studies some of the above problems, screens and optimises some wireless communication radar imaging algorithms and analyses and verifies them through experiments. The video-based back projection algorithm proposed in this paper has a recognition accuracy of more than 99%, which verifies that the use of the rotating convolution unit still has a recognition gain rate of 0.49% for the lightweight network when all samples are used.

Acknowledgements

This work was supported by Science and Technology Key Project of Shaanxi Science and Technology Department, China 2020GY091. This work was supported by Serving Local Special Project of Shaanxi Education Department, China 21JC002. This work was supported by Doctoral Scientific Research Foundation of Shaanxi University of Science and Technology, China 2020BJ-49, 2020J01. The Project supported by Natural Science Basic Research Plan in Shaanxi Province of China, Program No. 2023-JC-YB-484. Special Scientific Research Project of Shaanxi Provincial Department of Education Grant: 21JK0548.

References

Banerjee, S., Hempel, M. and Sharif, H. (2016) 'A survey of wireless communication technologies & their performance for high speed railways', *Journal of Transportation Technologies*, Vol. 6, No. 1, pp.15–29.

Bichi, B.Y., Islam, S.U. and Kademi, A.M. et al. (2022) 'An energy-aware application module for the fog-based internet of military things', *Discover Internet of Things*, Vol. 2, No. 4.

Comite, D., Ahmad, F. and Liao, D.H. et al. (2017) 'Multiview imaging for low-signature target detection in rough-surface clutter environment', *IEEE Transactions on Geoscience and Remote Sensing*, No. 9, pp.1–10.

García-Rial, F., Montesano, D. and Perez-Eijo, L. et al. (2020) 'Evaluation of standoff multistatic 3-D radar imaging at 300GHz', *IEEE Transactions on Terahertz Science and Technology*, Vol. 10, No. 1, pp.58–67.

Jiang, T., Mao, S. and Zhang, Z. et al. (2016) 'Editorial: special issue on 'next generation wireless communication technologies', *Digital Communications and Networks*, Vol. 2, No. 4, pp.159–161.

Kang, L., Cheng, Y. and Xiang, L. et al. (2016) 'Study on the theory and method of vortex-electromagnetic-wave-based radar imaging', *Iet Microwaves Antennas and Propagation*, Vol. 10, No. 9, pp.961–968.

Li, J., Gong, T. and Yang, S. et al. (2017) 'Influence of hypersonic turbulence in plasma sheath on synthetic aperture radar imaging', *IET Microwaves Antennas and Propagation*, Vol. 11, No. 15, pp.2223–2227.

Liu, H., Xu, W. and Bo J. et al. (2016) 'Wideband MIMO radar waveform design for multiple target imaging', *IEEE Sensors Journal*, Vol. 16, No. 23, pp.8545–8556.

Long, T., Liang, Z. and Liu, Q. (2019) 'Advanced technology of high-resolution radar: target detection, tracking, imaging, and recognition', *Science China Information Sciences*, Vol. 62, No. 4, pp.1–26.

Narayanan, R., Allebach, J. and Himed, B. (2019) 'Comparison of noise and chirp waveforms for radar target detection in clutter', *IET Radar, Sonar and Navigation*, Vol. 13, No. 8, pp.1333–1343.

Ng, W.H., Tran, H.T. and Martorella, M. et al. (2017) 'Estimation of the total rotational velocity of a non-cooperative target with a high cross-range resolution three-dimensional interferometric inverse synthetic aperture radar system', *Iet Radar Sonar and Navigation*, Vol. 11, No. 6, pp.1020–1029.

Peng, P., Guo, L.X. and Chen, B. et al. (2019) 'SAR imaging model of low-flying airplane target at complex maritime scene', *The Journal of Engineering*, Vol. 19, pp.5475–5477.

Qian, W., Hanchen, Y.U. and Zhang, Y. (2018) 'Inverse synthetic aperture radar imaging via covariance compressive sensing', *Guofang Keji Daxue Xuebao/Journal of National University of Defense Technology*, Vol. 40, No. 3, pp.95–100.

Singh, P., Shankar, A. and Diwakar, M. (2022) 'Review on nontraditional perspectives of synthetic aperture radar image despeckling', *Journal of Electronic Imaging*, Vol. 32, No. 2.

Smys, S., Bestak, R. and Chen, I.Z. et al. (2019) 'Target localization algorithm in a three-dimensional wireless sensor networks', *Proceedings of the International Conference on Computer Networks and Communication Technologies*, Vol. 15, No. 5, pp.33–42. Doi: 10.1007/978-981-10-8681-6_5.

Sun, Y., Chen, L. and Qu, L. (2019) 'Through-the-wall radar imaging algorithm for moving target under wall parameter uncertainties', *IET Image Processing*, Vol. 13, No. 11, pp.1903–1908.

Tang, V.H., Bouzerdoum, A. and Phung, S.L. et al. (2017) 'A sparse Bayesian learning approach for through-wall radar imaging of stationary targets', *IEEE Transactions on Aerospace and Electronic Systems*, Vol. 99, pp.1–1.

Wang, L., Wang, J. and Sun, L. (2018) 'Evaluation of trajectory error effects in BP based space target ISAR imaging', *Transactions of Nanjing University of Aeronautics and Astronautics*, Vol. 35, No. 6, pp.5–15.

Wang, Y. and Chen, X. (2019) 'Three-dimensional interferometric ISAR sensors imaging for the ship target with two-dimensional sparsity', *Journal of Harbin Institute of Technology*, Vol. 26, No. 2, pp.23–35.

Yang, J., Su, W. and Gu, H. (2016) 'High-resolution multiple-input–multiple-output–inverse synthetic aperture radar imaging based on sparse representation', *IET Radar Sonar and Navigation*, Vol. 10, No. 7, pp.1277–1285.

Yong, W. and Li, X. (2016) 'Three-dimensional interferometric ISAR imaging for the ship target under the bi-static configuration', *IEEE Journal of Selected Topics in Applied Earth Observations and Remote Sensing*, Vol. 9, No. 4, pp.1–16.

Yong, W., Xu, R. and Zhang, Q. et al. (2017) 'ISAR imaging of maneuvering target based on the quadratic frequency modulated signal model with time-varying amplitude', *IEEE Journal of Selected Topics in Applied Earth Observations and Remote Sensing*, Vol. 3, pp.1–13.

Yurduseven, O., Cooper, K. and Chattopadhyay, G. (2019) 'Point-spread-function (PSF) characterization of a 340-GHz imaging radar using acoustic levitation', *IEEE Transactions on Terahertz Science and Technology*, Vol. 9, No. 1, pp.20–26.

Zhang, Q., Di, M. and Ying L. et al. (2018) 'Dwell scheduling algorithm for digital array radar', *Journal of Beijing Institute of Technology*, Vol. 27, No. 95, No. 1, pp.78–86.